

# Fracture in tension–compression-asymmetry solids via phase field modeling

Gang Zhang<sup>a</sup>, Tian Fu Guo<sup>b</sup>, Xu Guo<sup>c,d,\*</sup>, Shan Tang<sup>c,d,\*</sup>, Mark Fleming<sup>e</sup>, Wing Kam Liu<sup>e</sup>

<sup>a</sup> School of Mechanical and Electrical Engineering, Wuhan Institute of Technology, Wuhan, 430200, PR China

<sup>b</sup> Institute of High Performance Computing, A\*STAR, Singapore, 138632, Singapore

<sup>c</sup> State Key Laboratory of Structural Analysis for Industrial Equipment, Department of Engineering Mechanics, Dalian University of Technology, Dalian, 116023, PR China

<sup>d</sup> International Research Center for Computational Mechanics, Dalian University of Technology, PR China

<sup>e</sup> Department of Mechanical Engineering, Northwestern University, Evanston, IL 60208, USA

Received 18 March 2019; received in revised form 27 June 2019; accepted 1 August 2019

Available online 28 August 2019

## Highlights

- A phase field model is built to model the fracture of tension-compression-asymmetry solids.
- The stress singularity around the crack tip is greatly influenced by the ratio of tensile modulus to compressive modulus.
- The hardening of the material can delay the fracture with more diffusive fracture process zone.

## Abstract

Many nonlinear elastic materials exhibit an asymmetric response when loaded in tension versus compression. In this paper, we study the fracture of such nonlinearly elastic materials with tension–compression asymmetry by virtue of phase field modeling. An additive decomposition of strain energy is utilized and extended to account for the modulus difference between tension and compression. This strain energy decomposition is demonstrated for both a neo-Hookean model and an Odgen model. The decomposition is proven to be consistent with the basic requirements of thermodynamics and is important for fracture modeling under the stress states with both compression and tension. The implementation of the phase field model with both decomposed energy of neo-Hookean and Odgen model is given. The implemented model is capable of capturing the tension–compression asymmetry of nonlinear elastic solids. It also can model crack initiation and propagation efficiently especially when the material undergoes both tension and compression, demonstrated through several typical specimens with pre-set crack. The stress fields around the crack tip break the classical law of singularity for the elastic solids with tension–compression symmetry ( $\sigma \propto r^{-0.5}$ ), which is greatly influenced by the ratio of tensile modulus to compressive modulus. The hardening of the material can delay the fracture with more diffusive fracture process zone, demonstrated by the modified Odgen

\* Correspondence to: Department of Engineering Mechanics, Dalian University of Technology, Dalian, China.

E-mail addresses: [guoxu@dlut.edu.cn](mailto:guoxu@dlut.edu.cn) (X. Guo), [shantang@dlut.edu.cn](mailto:shantang@dlut.edu.cn) (S. Tang).

model. The proposed approach shows a great potential to predict the damage behavior of the materials with tension–compression asymmetry at finite strain.

© 2019 Elsevier B.V. All rights reserved.

**Keywords:** Nonlinear elastic materials; Fracture; Phase field; Tension–compression asymmetry; Soft tissue

## 1. Introduction

Many natural or synthetic materials exhibit different behavior when loaded in tension and compression. This phenomenon, known as tension–compression asymmetry, is an issue when analyzing such materials as biomaterials like brain tissues, and engineering polymeric materials like PET (Polyethylene terephthalate). For these materials, the tensile modulus can be much different than the compressive modulus [1–10]. The fracture of this type of material has attracted great attention and accurate modeling of fracture is important when using it for either medical or structural applications [9,11–16].

Past research has developed mathematical models to describe the mechanical behavior of materials with tension–compression asymmetry. The pioneering work of Ambartsumyan is summarized in the monograph on bi-modulus elasticity theory [17–19]. The constitutive relation proposed by the original work of Ambartsumyan has been further developed recently. Du and Guo [20] and Du et al. [21] established a series of variational principles and the related bounding theorems for bi-modulus materials. These variational principles can help to obtain the effective overall properties of heterogeneous materials with bi-modulus constituents in a variationally consistent way. However, these theoretical and numerical formulations are confined to small deformations, and do not account for the material behaviors at finite strains. Recent works of Budday et al. [9,10] have tried to employ the Ogden model through modifying model parameter  $\alpha$ . However, the asymmetry predicted by the proposed model still remains less pronounced than that observed in their experiments.

The phase-field approach to modeling fracture has gained considerable attention in recent years. This approach, also known as the variational approach to fracture, is able to capture complex crack patterns, such as curved crack, without having to model the discontinuity directly (see in Fig. 1). This approach was first proposed by Francfort and Marigo [22]. An alternative framework is formulated by Miehe et al. [23,24] based on continuum mechanics and thermodynamic arguments. The decomposition of the elastic strain energy into tensile and compressive parts is considered by Amor et al. [25], who decomposed the elastic energy into volumetric and deviatoric parts to distinguish the tensile and compressive contributions to fracture at the small deformation regime, while Miehe et al. [23] took into account the contribution of the principal strains. These approaches also have been further developed by other researchers, including [26–30].

To the best of our knowledge, the fracture of the materials with tension–compression asymmetry at finite strain has not been studied and multiple challenges still remain. First, the explicit form of the energy potential for bi-modulus materials remains elusive, even for materials in the small deformation regime. Second, the energy decomposition which accounts for the differential contributions of tension and compression is not straightforward at finite strain. Inspired by Miehe et al. [23] and Borden et al. [29], we previously proposed a novel method to decompose the strain energy into two parts, the principal stretch and volumetric deformation [31]. However, identical tension and compression moduli were assumed. The same assumption is also adopted by all the previous phase field models for fracture, to our knowledge. When the tensile behavior differs from the compressive behavior, the proposed model should be consistent with thermodynamics laws, which is satisfied by classical hyperelastic models such as neo-Hookean and Ogden models. It should be noted that the Ogden model appears better suited for mechanical modeling of brain tissue [9,10]. Only the energy decomposition of neo-Hookean model was considered in our previous work [31]. It will be shown in the present work that the energy decomposition can also be applied to Ogden model. In our viewpoint, the strain energy decomposition not only increases numerical stability for phase field modeling of fracture, but also opens an avenue to model the materials with tension–compression asymmetry.

The present work extends the previous works in the small deformation regime to simulate the fracture of materials with tension–compression asymmetry undergoing finite deformation. The paper is organized as follows. In Section 2, a finite deformation elasticity model with tension–compression asymmetry is proposed, which is based on the neo-Hookean model, and is consistent with the laws of thermodynamics. In Section 3, based on the

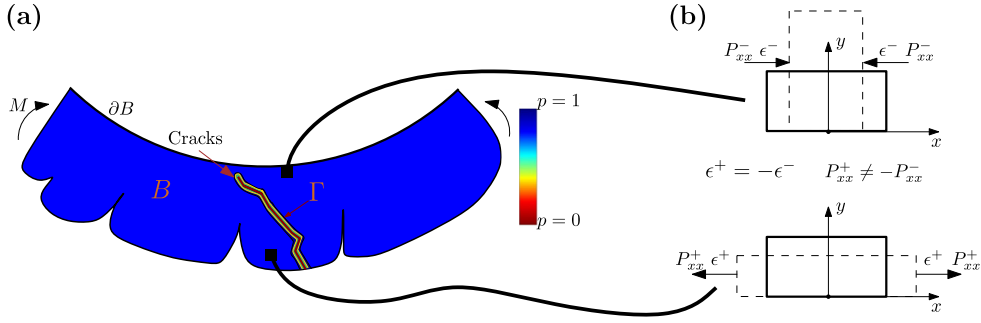


**Fig. 1.** (a) Schematic representation of a solid body  $B$  enclosed by its boundary denoted by  $\partial B$ , where the solid material exhibits tension–compression asymmetry. The internal discontinuity is approximated by the phase field  $p$  ranging from  $p = 1$  for intact to  $p = 0$  for fracture. (b) Schematic illustration of the material behavior with tension–compression asymmetry. At different material points, the stress states (tension or compression is dominated) can cause a different mechanical response.

proposed strain energy with tension–compression asymmetry, we will embed it into the framework of the phase field modeling of fracture. We study the behavior of the proposed model for fracture by performing a number of numerical experiments. Our results show that the current approach is very stable numerically. We also demonstrate a different crack tip stress field, distinguished from the classical elastic solids with tension–compression symmetry. The Odgen model is also extended to be embedded into the phase field framework. A different fracture behavior can be observed. The proposed approach paves a new way to model the fracture of the nonlinear elastic materials with tension–compression asymmetry in engineering applications.

## 2. Nonlinear tension–compression asymmetry model

Linear elasticity models with tension–compression asymmetry have been previously developed, as discussed in the Introduction. The present work is focused on the nonlinear elastic materials with tension–compression asymmetry. It should be noted that viscoelastic effects which may be present in biomaterials such as brain tissue are not included in the present paper. However, viscoelasticity can be considered through models such as [32,33], and [34].

Let us consider an arbitrary body  $B$  enclosed by the surface  $\partial B$  (see Fig. 1). During deformation, a point  $X$  in the undeformed reference configuration is mapped to  $\mathbf{x}$  in the current deformed configuration by the deformation gradient  $\mathbf{F}$ . The right Cauchy–Green tensor is defined as

$$\mathbf{C} = \mathbf{F}^T \mathbf{F} = \mathbf{Q} \mathbf{\Lambda} \mathbf{Q}^T$$

where  $\mathbf{Q}$  consists of the orthogonal eigenvectors of  $\mathbf{C}$  and  $\mathbf{\Lambda} = \text{diag}(\lambda_1^2, \lambda_2^2, \lambda_3^2)$  is a diagonal matrix of principal right Cauchy–Green tensor and  $\lambda_i, i = 1 \dots 3$  are the principal stretches. Suppose  $a_m|_{m=1..3}$  are the eigenvalues of  $\mathbf{C}$ , then the following equation can be proven:

$$\frac{da_m}{d\mathbf{C}} = \mathbf{a}_m \otimes \mathbf{a}_m$$

where  $\mathbf{a}_m$  is the eigenvector corresponding to the eigenvalue  $a_m$  [35,36]. As we know,  $a_m = \lambda_m^2$  is the eigenvalue of  $\mathbf{C}$ .

### 2.1. Nonlinear elasticity with tension–compression asymmetry

Numerous models have been developed to model for nonlinear elasticity. We adopt the compressive neo-Hookean model as a prototype, and then extend the present approach to an Odgen model, which is commonly used to model the mechanical behavior of human brain tissue.

In order to distinguish between tension and compression in this formulation, a tension/compression dependent shear modulus is defined as

$$\mu(\lambda_i) = \begin{cases} \mu^+, & \lambda_i > 1 \\ \mu^-, & \lambda_i \leq 1 \end{cases}$$

and a tension/compression dependent bulk modulus is defined as

$$K(J) = \begin{cases} K^+, & J > 1 \\ K^-, & J \leq 1 \end{cases}$$

where  $J = \det(\mathbf{F}) = \lambda_1 \lambda_2 \lambda_3$ . Using this form of the shear modulus and bulk modulus, the strain energy of the original neo-Hookean model can be rewritten in the following form, which considers the tension–compression asymmetry:

$$W = W_1 + W_2$$

where

$$W_1 = \sum_{i=1}^3 \mu(\lambda_i) \left[ \frac{1}{2} (\lambda_i^2 - 1) - \ln \lambda_i \right], \quad W_2 = \frac{1}{2} K(J) (\ln J)^2$$

The strain energy density  $W$  is always positive for an arbitrary deformation gradient  $\mathbf{F}$ . We define

$$\Pi(\lambda_i) = \frac{1}{2} (\lambda_i^2 - 1) - \ln \lambda_i.$$

such that

$$\Pi(\lambda_i)|_{\lambda_i=1} = 0$$

and

$$\frac{d\Pi(\lambda_i)}{d\lambda_i} = \lambda_i - \frac{1}{\lambda_i} = \begin{cases} > 0, & \lambda_i > 1 \\ \leq 0, & \lambda_i \leq 1 \end{cases}$$

Since  $\mu(\lambda_i) > 0$  and  $K(J) \geq 0$ , then  $W_1 \geq 0$ ,  $W_2 \geq 0$ , and hence  $W = W_1 + W_2 \geq 0$ .

$W_1$  can be reformulated as

$$W_1 = \sum_{i=1}^3 \mu(a_i) \left[ \frac{1}{2} (a_i - 1) - \frac{1}{2} \ln a_i \right]$$

by replacing  $\lambda_i^2$  with  $a_i$ . The first Piola–Kirchhoff stress can be obtained as

$$\begin{aligned} P_{iJ} &= \frac{\partial W}{\partial F_{iJ}} = \frac{\partial W_1}{\partial a_m} \frac{\partial a_m}{\partial C_{KL}} \frac{\partial C_{KL}}{\partial F_{iJ}} + \frac{\partial W_2}{\partial J} J F_{iJ}^{-T} \\ &= 2 \frac{\partial W_1}{\partial a_m} (a_m)_J (a_m)_L F_{iL} + \frac{\partial W_2}{\partial J} J F_{iJ}^{-T} \end{aligned}$$

where

$$\frac{\partial W_1}{\partial a_m} = \frac{1}{2} \mu(a_m) \left( 1 - \frac{1}{a_m} \right)$$

and

$$\frac{\partial W_2}{\partial J} = K(J) \frac{\ln J}{J}$$

It is evident that  $\frac{\partial W_1}{\partial a_m} \Big|_{a_m=1} = 0$  and  $\frac{\partial W_2}{\partial J} \Big|_{J=1} = 0$ , which results in zero stress in the undeformed configuration:

$$P_{iJ} \Big|_{\lambda_i=1, J=1} = 0$$

**Remark.** Other nonlinear elastic models can be similarly extended to account for tension–compression asymmetry. For example, the Ogden model, which is widely used to model brain tissue, can be modified as follows to account for tension–compression asymmetry

$$W = \sum_{i=1}^3 \left\{ \frac{2\mu(\lambda_i)}{\alpha^2} (\lambda_i^\alpha - 1 - \alpha \ln \lambda_i) \right\} + \frac{K(J)}{2} (\ln J)^2 \quad (1)$$

where  $\alpha$  is a material constant in the original Odgen model. We can prove in the same way as for the neo-Hookean model that  $W \geq 0$  and that the stress is zero in the undeformed reference configuration. Note that when  $\alpha = 2$  and  $\mu(\lambda_i) \equiv \mu$ , the Odgen model reduces to the neo-Hookean model.

### 3. Phase field formulation for fracture modeling

A phase field formulation is utilized to model fracture. The internal discontinuity surfaces,  $\Gamma$ , represent a set of discrete cracks. In accordance with Griffith's theory of fracture, the energy required to create a unit area of fracture surface is equal to the critical fracture energy density  $\mathcal{G}_c$ . To circumvent the problems associated with numerically tracking the discontinuity of a crack, the fracture surface  $\Gamma$  is modeled using a phase field,  $p(X, t)$

$$\begin{aligned} \int_{\Gamma} \mathcal{G}_c dS &= \int_B G_{\text{phase}}(p, \nabla p) dX \\ &= \int_B \mathcal{G}_c \left[ \frac{(p-1)^2}{4\ell} + \ell \frac{\partial p}{\partial X_I} \frac{\partial p}{\partial X_I} \right] dX \end{aligned} \quad (2)$$

where  $\ell$  is a model parameter that controls the width of the smooth approximation of the crack. Unless otherwise stated, we adopt the Lagrangian coordinates and all integrations are carried out in the undeformed reference configuration.

A phase field  $p$  is used to model the fracture process zone in nonlinear elastic solids with tension–compression asymmetry. Physically, the phase field quantifies the loss of material stiffness in the failure zone. Inspired by the work of Miehe et al. [23] and Borden et al. [29] for small deformation elasticity, we adopt the following form of free energy  $G_{\text{asym}}$  (coupled with  $p$ ) for solids with tension–compression asymmetry:

$$G_{\text{asym}} = [(1 - \mathcal{K}) p^2 + \mathcal{K}] W^+ + W^- \quad (3)$$

The model parameter  $\mathcal{K}(\ll 1)$  is introduced to achieve better numerical stability. For linear elastic materials, the parameter  $\mathcal{K}$  has been shown to be unnecessary by Borden et al. [29]. However, for non-linear materials, our numerical experience indicates the efficacy of a non-zero  $\mathcal{K}$ . As shown in previous publications, [31], the phase field damage-coupled energy refers to strain energy with tensile stretching

$$W^+ = W(\lambda_i^+, J^+) \quad \text{where } \lambda_i^+ = \begin{cases} \lambda_i & \text{for } \lambda_i > 1 \\ 1 & \text{for } \lambda_i \leq 1 \end{cases} \quad J^+ = \begin{cases} J & \text{If } J > 1 \\ 1 & \text{If } J \leq 1 \end{cases}$$

On the contrary, the strain energy with compressive stretching is

$$W^- = W(\lambda_i^-, J^-) \quad \text{where } \lambda_i^- = \begin{cases} \lambda_i & \text{for } \lambda_i < 1 \\ 1 & \text{for } \lambda_i \geq 1 \end{cases} \quad J^- = \begin{cases} J & \text{If } J < 1 \\ 1 & \text{If } J \geq 1 \end{cases}$$

This decomposition can strictly satisfy the condition:

$$W = W^+ + W^-$$

when there is no damage ( $p = 1$ ). The total potential energy of the body  $U$ , composed of the elastic energy and the fracture energy, is then given by

$$U = \int_B G_{\text{asym}} dX + \int_B G_{\text{phase}}(p, \nabla p) dX \quad (4)$$

with  $G_{\text{phase}}$  previously defined by the integrand in (Eq. (2)). The kinetic energy of the body  $B$  is

$$T = \frac{1}{2} \int_B \rho_0 \dot{x}_i \dot{x}_i dX \quad (5)$$

where  $\rho_0$  is the initial mass density. The Lagrangian for the elastic problem under study reads

$$L(\mathbf{x}, \dot{\mathbf{x}}, p) = T(\dot{\mathbf{x}}) - U(\mathbf{x}, p) = \int_B \hat{L} dX$$

Variation of  $\hat{L}$  gives

$$\begin{aligned}\delta \hat{L} &= \rho_0 \dot{x}_i \delta \dot{x}_i - \frac{\partial G_{\text{asym}}}{\partial F_{iJ}} \delta x_{i,J} - \frac{\partial G_{\text{asym}}}{\partial p} \delta p - \delta G_{\text{phase}} \\ &= \frac{d}{dt} (\rho_0 \dot{x}_i \delta x_i) - \left( \frac{\partial G_{\text{asym}}}{\partial F_{iJ}} \delta x_i \right)_{,J} - \frac{\partial G_{\text{asym}}}{\partial p} \delta p + \left[ \left( \frac{\partial G_{\text{asym}}}{\partial F_{iJ}} \right)_{,J} - \rho_0 \ddot{x}_i \right] \delta x_i - \delta G_{\text{phase}}\end{aligned}\quad (6)$$

where

$$\frac{\partial G_{\text{asym}}}{\partial p} = 2(1 - \mathcal{K}) p W^+,$$

and the first Piola–Kirchhoff stress with damage is:

$$P_{iJ} = \frac{\partial G_{\text{asym}}}{\partial F_{iJ}} = [(1 - \mathcal{K}) p^2 + \mathcal{K}] \frac{\partial W^+}{\partial F_{iJ}} + \frac{\partial W^-}{\partial F_{iJ}}$$

where

$$\frac{\partial W^+}{\partial F_{iJ}} = \sum_{i=1}^3 \frac{\partial W^+}{\partial \lambda_i^+} \frac{\partial \lambda_i^+}{\partial F_{iJ}} + \frac{\partial W^+}{\partial J^+} \frac{\partial J^+}{\partial F_{iJ}}, \quad \frac{\partial W^-}{\partial F_{iJ}} = \sum_{i=1}^3 \frac{\partial W^-}{\partial \lambda_i^-} \frac{\partial \lambda_i^-}{\partial F_{iJ}} + \frac{\partial W^-}{\partial J^-} \frac{\partial J^-}{\partial F_{iJ}}$$

with

$$\begin{aligned}\frac{\partial \lambda_i^+}{\partial F_{iJ}} &= \begin{cases} \frac{\partial \lambda_i}{\partial F_{iJ}} & \text{for } \lambda_i > 1 \\ 0 & \text{for } \lambda_i \leq 1 \end{cases}, \quad \frac{\partial \lambda_i^-}{\partial F_{iJ}} = \begin{cases} \frac{\partial \lambda_i}{\partial F_{iJ}} & \text{for } \lambda_i < 1 \\ 0 & \text{for } \lambda_i \geq 1 \end{cases} \\ \frac{\partial J^+}{\partial F_{iJ}} &= \begin{cases} \frac{\partial J}{\partial F_{iJ}} & \text{for } J > 1 \\ 0 & \text{for } J \leq 1 \end{cases}, \quad \frac{\partial J^-}{\partial F_{iJ}} = \begin{cases} \frac{\partial J}{\partial F_{iJ}} & \text{for } J < 1 \\ 0 & \text{for } J \geq 1 \end{cases}\end{aligned}$$

and

$$\delta G_{\text{phase}} = \frac{\partial G_{\text{phase}}}{\partial p} \delta p = \left( 2\ell \mathcal{G}_c \frac{\partial p}{\partial X_I} \delta p \right)_{,I} + \left( \mathcal{G}_c \frac{p-1}{2\ell} - 2\ell \mathcal{G}_c \frac{\partial^2 p}{\partial X_I^2} \right) \delta p$$

Setting  $\delta L = 0$  leads to

$$\frac{\partial P_{iJ}}{\partial X_J} = \rho_0 \ddot{x}_i, \quad (7)$$

$$[4\ell(1 - \mathcal{K}) W^+ + \mathcal{G}_c] p - 4\mathcal{G}_c \ell^2 \frac{\partial^2 p}{\partial X_I^2} = \mathcal{G}_c, \quad (8)$$

with natural boundary conditions

$$p_{,I} N_I = 0 \quad (9)$$

$$P_{iJ} N_J = t_i \quad (10)$$

where  $t_i$  is the traction prescribed on the outer surface  $\partial B$  with the normal vector  $N$ . Under plane strain conditions, the implementation of the above equations can be greatly simplified [31].

#### 4. Numerical formulation

The numerical solution of Eqs. (7)–(8) with the finite element method requires both spatial and temporal discretization. In this section, we formulate the spatial discretization with the Galerkin method. We also introduce a staggered scheme to solve the coupling equations. Although it is natural to consider the inertial effects through our proposed scheme, they are ignored in the present paper for simplicity.

For a weak form of the problem we define the trial solution spaces  $\mathcal{S}_t$  for the displacements  $\mathbf{u}$  and  $\hat{\mathcal{S}}_t$  for the phase field  $p$  :

$$\begin{aligned}\mathcal{S}_t &= \left\{ \mathbf{u}(t) \in (H^1(B))^d \mid u_i(t) = g_i \text{ on } \partial B \right\} \\ \hat{\mathcal{S}}_t &= \{p(t) \in (H^1(B))\}\end{aligned}$$

where superscript  $d$  represents the dimension. Similarly, the weighting function spaces are defined as

$$\begin{aligned}\mathcal{V} &= \left\{ \mathbf{w} \in (H^1(B))^d \mid w_i = 0 \text{ on } \partial B \right\} \\ \hat{\mathcal{S}}_t &= \{q \in (H^1(B))\}\end{aligned}$$

Multiplying the Eqs. (7), (8) by the appropriate weighting functions and applying integration by parts leads to the weak formulation:

$$\int_B P_{iJ} \frac{\partial w_i}{\partial X_J} dX - \int_{\partial B} P_{iJ} N_J w_i dS = 0 \quad (11)$$

$$\int_B \left[ 2(1 - \mathcal{K}) p W^+ q + \frac{\mathcal{G}_c (p - 1) q}{2\ell} + 2\mathcal{G}_c \ell \frac{\partial q}{\partial X_I} \frac{\partial p}{\partial X_I} \right] dX = 0 \quad (12)$$

As mentioned previously,  $\mathcal{K}$  is a parameter which improves numerical stability. It should be a small positive value.

Given the initial and boundary conditions, we need to find  $\mathbf{u}(X, t) \in \mathcal{S}_t$  and  $p(X, t) \in \hat{\mathcal{S}}_t$  such that Eqs. (11), (12) are satisfied for all  $\mathbf{w} \in \mathcal{V}$ ,  $q \in \hat{\mathcal{S}}_t$ .  $\mathbf{u}(X, t) \in \mathcal{S}_t$  and  $p(X, t) \in \hat{\mathcal{S}}_t$ . Both the finite dimensional trial solution and weighting function spaces are interpolated by the nodal values and the same set of linear basis functions.

We then apply the staggered time discretization scheme to solve Eqs. (11)–(12). In the present approach, the momentum equation (Eq. (11)) and the phase fields are solved independently (Eq. (12)). That is, at a given time step, the momentum equation is solved first to update the displacement. With the updated displacements, the phase field is solved. Our numerical practice indicates that solving the momentum equation and the phase field at the same time can cause some numerical issues. The staggered solution scheme reduces the original problem into two smaller systems, resulting in increased flexibility and numerical stability while maintaining solution accuracy. The proposed algorithm is summarized in [Box I](#) in [Appendix](#).

## 5. Numerical results

Several numerical examples are presented to demonstrate the ability of the proposed phase field model on the fracture of nonlinear elastic materials with tension–compression asymmetry. All the geometries are discretized spatially using  $C^0$ -continuous finite elements. We adopt the staggered solution strategy present in the previous section. Unless otherwise stated, in all our simulations,  $\mu^+$  and  $K^+$  are fixed and  $\mu^-$  and  $K^-$  are varied. The bulk modulus ratio  $K^+/K^-$  is same as the shear modulus ratio  $\mu^+/\mu^-$ . Simulation cases are identified by C1, C2, C3, C4 and C5 for ease of illustration.

We first consider the analysis of a fracture in a plane strain three-point bend specimen (Marked as C1). The geometry for a beam with a straight vertical notch is shown in [Fig. 2a](#), along with the boundary conditions and the finite element mesh of the problem. The beam is discretized with 15412 linear triangular elements and 7901 nodes, following a mesh convergence study. Computations are performed in a displacement-driven context. Both the  $x$  and  $y$  degrees-of-freedom at the two supports are fixed.

[Fig. 2b](#) shows the reaction force,  $F_R$ , as a function of normalized displacement,  $u/H$ , for five ratios of the tension to compression modulus ( $\mu^+/\mu^- = 0.2, 0.5, 1.0, 2.0, 5.0$ ). The length scale is set as  $\ell = 0.02$  mm, the normalized fracture energy  $\mathcal{G}_c/(\mu^+\ell) = 2.016$  and  $\mathcal{K} = 0.001$ . The shear modulus and bulk modulus are chosen as  $\mu^+ = 1.86$  MPa and  $K^+ = 18.0$  MPa, respectively. In general, the shape of the force vs. displacement curve is very similar to Miehe et al. [37] for three-point bending of thermo-elastic solids. When  $\mu^+/\mu^- = 1.0$ , the model can reduce to the phase field fracture of classical neo-Hookean solids, discussed in our recent work [31]. It can be observed in [Fig. 2b](#) that the force vs. displacement response is initially linear and the stiffness increases with decreasing  $\mu^+/\mu^-$ . When the displacement reaches a critical value, the force decreases rapidly due to the accumulation of the damage, as represented by the phase field. The critical displacements value increases with increasing  $\mu^+/\mu^-$ . It appears that a large compressive modulus  $\mu^-$  can promote the crack propagation, although

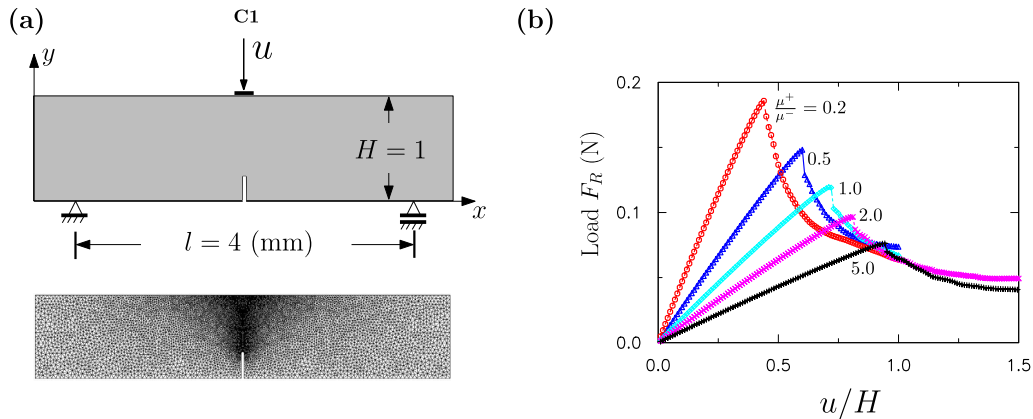


**Fig. 2.** Three-point bending simulations. (a) Geometry, boundary conditions and FE mesh. (b) The reaction force vs. normalized displacement under five different levels of *modulus ratio* (representing tension–compression asymmetry):  $\mu^+/\mu^- = 0.2, 0.5, 1.0, 2.0, 5.0$ . The modified neo-Hookean model with tension–compression asymmetry is employed.

further study on the fundamental physics of this observation needs to be carried out. Another interesting observation is that the force drops more rapidly with smaller  $\mu^+/\mu^-$ .

Fig. 3 shows the stress contours ( $P_{xx}$ ) on the deformed configuration under four modulus ratios  $\mu^+/\mu^- = 0.2, 0.5, 2.0, 5.0$  at the imposed displacement  $u/H = 0.9$ . The contour plots of the phase field are also shown on the undeformed configuration. As expected, the material in the top region of the block is compressed while stretched at the bottom. From the contour of crack phase field, it can be seen that the crack propagates in a straight line towards the top surface and the phase field is localized. For smaller  $\mu^+/\mu^-$ , the propagation of the crack occurs sooner, consistent with what observed in Fig. 2. As a result, the total length of crack propagation is longer for the same displacement level. The high stress field around the crack tip is localized and the high local stress moves with the crack tip as the crack propagates. Outside the crack region, the stress is much more uniform.

The proposed framework can model the nucleation of the fracture naturally. When the phase field at the tip of the preset crack drops to a small value (set as 0.01 in our cases), nucleation of a new crack occurs. Fig. 4 shows the contours of the phase field ( $p$ ) on the deformed configuration with two modulus ratios  $\mu^+/\mu^- = 5.0, 0.5$ . The new cracks nucleate when the imposed displacements are  $u/H = 0.97$  and  $0.61$  respectively, which causes the propagation of the preset crack.

The evolution of stress,  $P_{xx}$ , in the initial crack tip element as a function of the imposed displacement is plotted in Fig. 5a for five modulus ratios  $\mu^+/\mu^- = 0.2, 0.5, 1.0, 2.0, 5.0$ . The crack tip stress,  $P_{xx}$ , increases nonlinearly with the imposed displacement. When the damage is large, the crack propagates and structure loses the load bearing capability, resulting in a rapid drop of the stress. It can be seen from Fig. 5a that the maximum crack tip stress the specimen can sustain increases with smaller  $\mu^+/\mu^-$ . At the imposed displacement level  $u/H = 0.9$ , Fig. 5b plots the stress  $P_{xx}$  distribution vs. the distance to the initial crack tip  $r$  along the crack path for the same five modulus ratios as Fig. 5a. Under this imposed displacement level, the crack propagates for  $\mu^+/\mu^- = 0.2, 0.5, 1.0, 2.0$  and the stress has reduced to zero in the wake of the crack.

In classical linear elastic fracture mechanics, the crack tip stress field exhibits a  $1/\sqrt{r}$  singularity ( $\sigma \propto r^{-0.5}$ ). The stress singularity around the crack tip for  $\mu^+/\mu^- = 1.0$  is examined and is found to be approximately  $1/\sqrt{r}$ . It can be seen from Fig. 5b that the singularity of stress fields increases with decreasing  $\mu^+/\mu^-$ . The large  $\mu^+/\mu^-$  may be used to reduce the stress singularity at the crack tip. It appears that tension–compression asymmetry can greatly change the crack tip stress fields and its related fracture behavior. It should be noted that the stress fields vs. the distance to crack tip may be different when it is plotted in the current configuration. It is found in our work that the general trend is almost the same as that in the undeformed configuration although there is some quantitative difference. However, the current work is focused on computational methods for the phase field of fracture, and results are not included to make the illustration more concise.

After the detailed examination on the fracture under three-point bending, we now study the fracture in a rectangular plate of 2.0 mm width and 0.4 mm height with a horizontal pre-notch of 0.2 mm length at the center



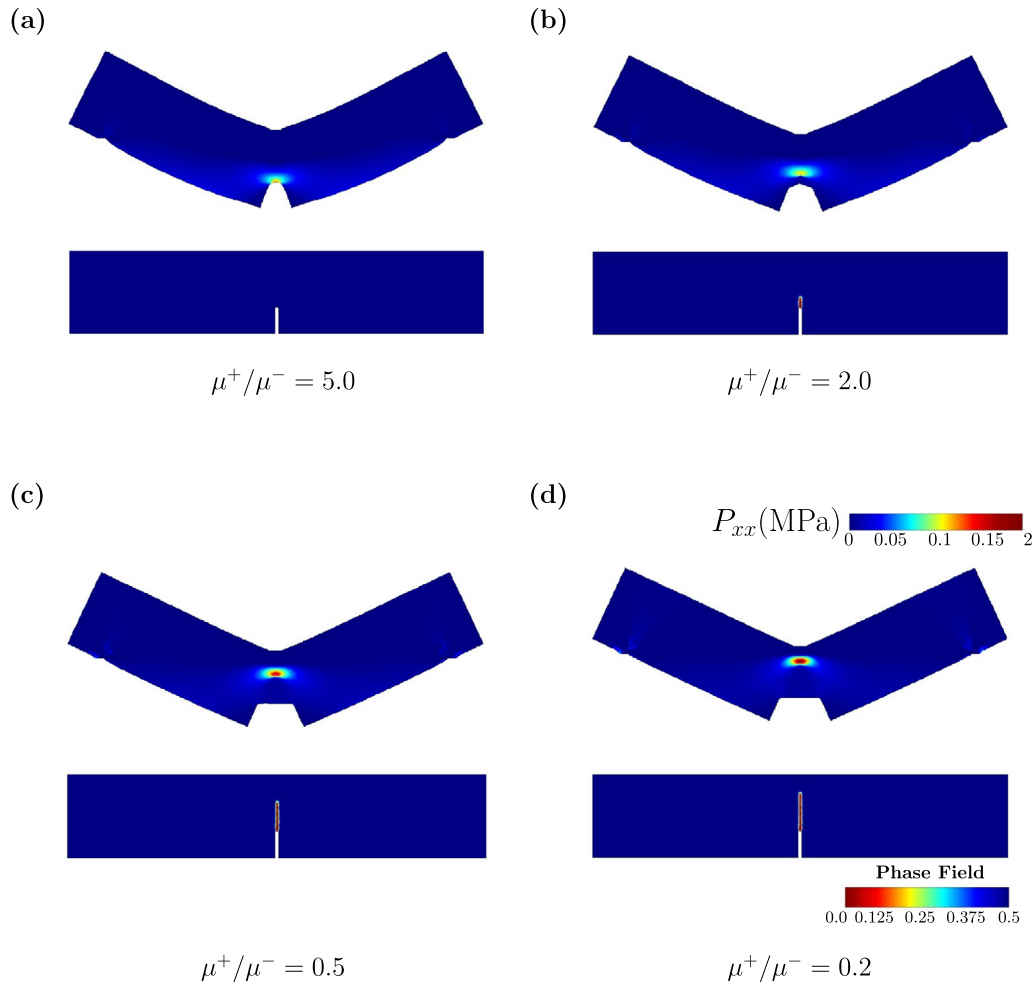


**Fig. 3.** The contour plots of stress ( $P_{xx}$ ) and phase field ( $p$ ) for three-point bending specimen in the current deformed and undeformed reference configurations respectively. The imposed displacement is  $u/H = 0.9$  with four levels of modulus ratio: (a)  $\mu^+/\mu^- = 5.0$ ; (b)  $\mu^+/\mu^- = 2.0$ ; (c)  $\mu^+/\mu^- = 0.5$ ; (d)  $\mu^+/\mu^- = 0.2$ . The modified neo-Hookean model with tension-compression asymmetry is employed.

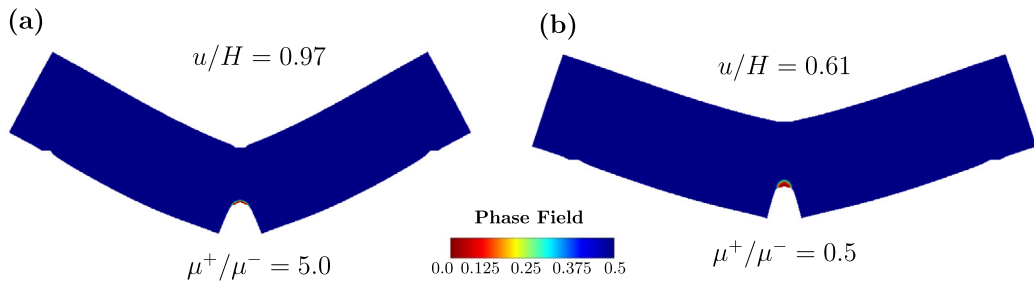


**Fig. 4.** The contour plots of phase field ( $p$ ) for three-point bending specimen in the current deformed configuration when the fracture initiates. The imposed displacement is  $u/H = 0.97$  and  $0.61$  with modulus ratios: (a)  $\mu^+/\mu^- = 5.0$ ; (b)  $\mu^+/\mu^- = 0.5$ . The modified neo-Hookean model with tension-compression asymmetry is employed.

under the tensile loading (Marked as C2). The geometric setup is shown in Fig. 6a. In order to capture the crack pattern properly, the mesh is refined around the pre-notch. The finite element mesh includes 9459 elements with the minimum element size 0.0057 mm and 4888 nodes, based on a mesh convergence study. The shear modulus

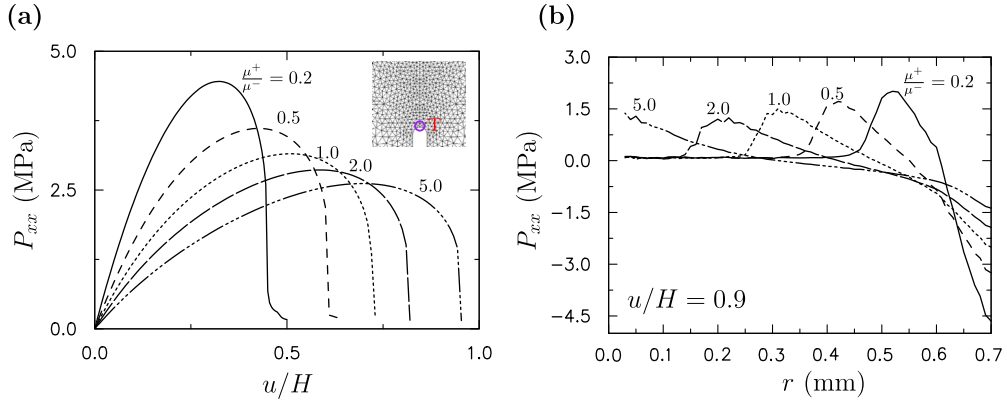


**Fig. 5.** (a) Nominal stress vs. normalized imposed displacement on the block for the element at the original crack tip under five levels of modulus ratios  $\mu^+/\mu^- = 0.2, 0.5, 1.0, 2.0, 5.0$ . The inset of the figure shows the location of the element. (b) Nominal stress distribution ahead of the initial crack tip under five levels of modulus ratios  $\mu^+/\mu^- = 0.2, 0.5, 1.0, 2.0, 5.0$  at the imposed displacement level  $u/H = 0.9$ . The modified neo-Hookean model with tension-compression asymmetry is employed.

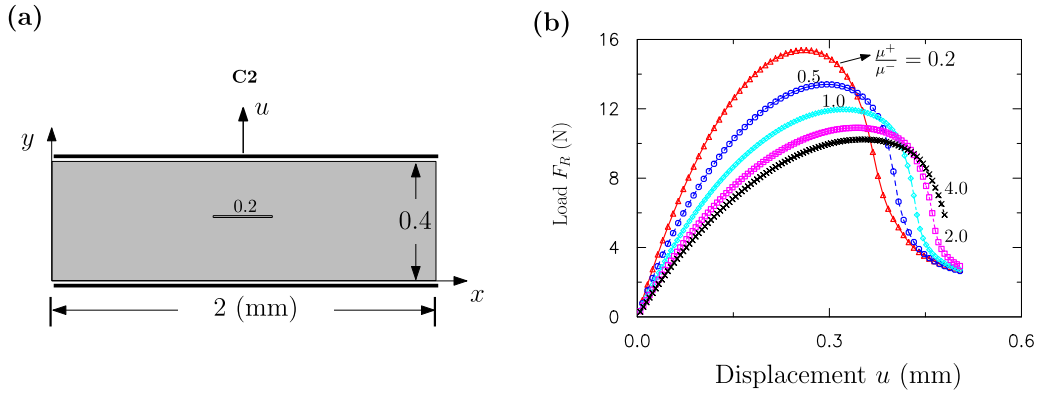


**Fig. 6.** Fracture of a rectangular plate with a centered pre-set notch under the imposed displacement  $u$ . (a) Geometry and boundary conditions and (b) model prediction of load-displacement curves under five levels of modulus ratio  $\mu^+/\mu^-$ . The modified neo-Hookean model with tension-compression asymmetry is employed.

and bulk modulus are chosen as  $\mu^+ = 5.24$  MPa and  $K^+ = 21.0$  MPa, respectively. The fracture toughness is set to  $\mathcal{G}_c = 1.5$  N/mm and  $\mathcal{K} = 0.001$ . A monotonic displacement is imposed on the top surface with the constant displacement increment  $\Delta u = 0.0016$  mm and the bottom is fixed in the  $y$  direction.

Fig. 6b plots the load-displacement curves calculated from the model shown in Fig. 6a under five levels of the shear modulus ratio  $\mu^+/\mu^-$ . The general response is very similar to those shown in our previous for neo-Hookean solids with  $\mu^+/\mu^- = 1.0$  and Miehe and Schänzel [38]. In the work of Miehe and Schänzel [38], a regularization parameter  $\eta$  is introduced to increase numerical stability. This artificial parameter can greatly change the softening behavior when the crack propagates. Due to the novel energy decomposition proposed in our previous work, we do not introduce any artificial parameters in the simulations. The similar trend of force response is also observed from Fig. 6b compared with those shown in Fig. 2b. That is, the lower shear modulus ratio  $\mu^+/\mu^-$  results in the higher force response and smaller strain level for crack initiation.

The contours of the nominal stress  $P_{yy}$  and the fracture phase fields are shown in Fig. 7a-d for four levels of modulus ratios  $\mu^+/\mu^- = 0.2, 0.5, 2.0, 4.0$  at the imposed displacement level  $u = 0.4$  mm. The obtained fracture pattern is consistent with the results in [38]. When  $\mu^+/\mu^-$  is smaller, crack propagation occurs earlier. In general, although the crack configuration of penny-shaped crack at the center of the specimen is different from that under three-point bending, the general trend looks similar.

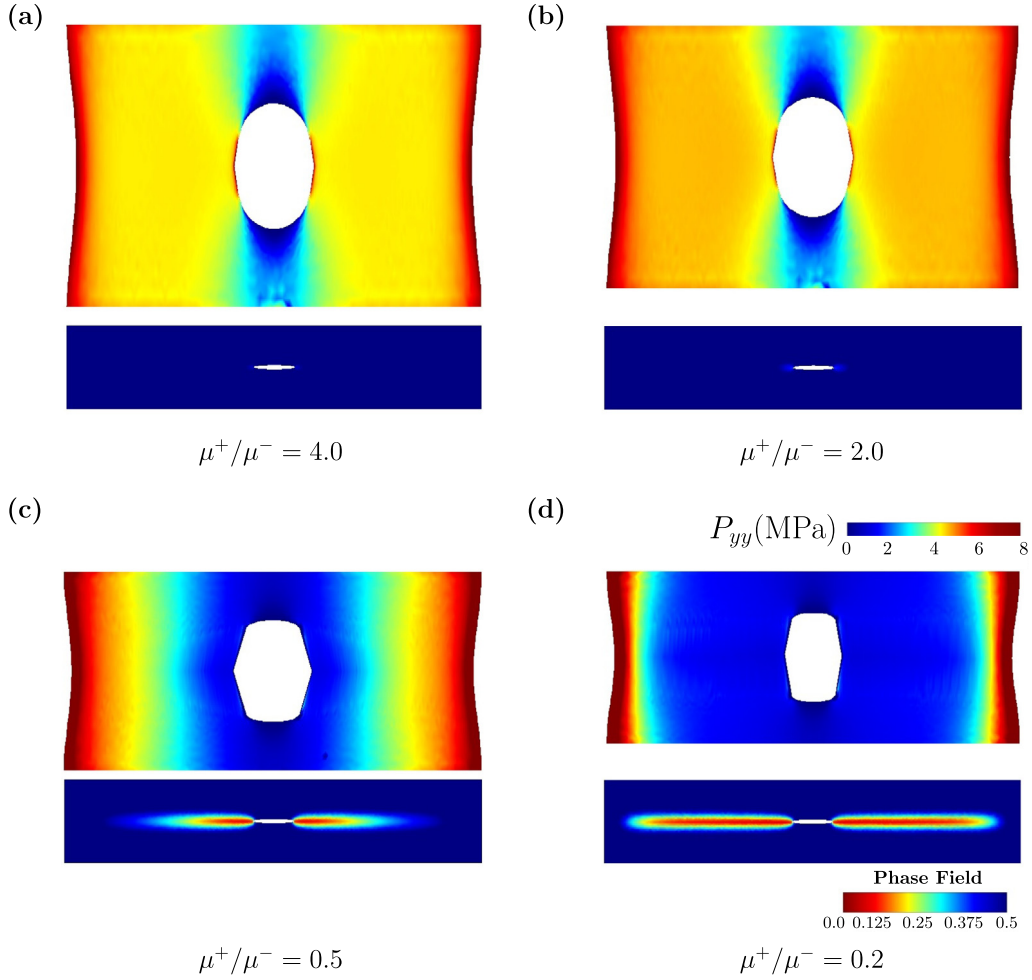


**Fig. 7.** The contour plots of stress  $P_{yy}$  and phase field  $p$  around the notch in the current deformed and undeformed reference configurations respectively, under four levels of modulus ratio  $\mu^+/\mu^-$  at the imposed displacement level  $u = 0.4$  mm. The modified neo-Hookean model with tension–compression asymmetry is employed: (a)  $\mu^+/\mu^- = 4.0$ ; (b)  $\mu^+/\mu^- = 2.0$ ; (c)  $\mu^+/\mu^- = 0.5$ ; (d)  $\mu^+/\mu^- = 0.2$ .

We next study the fracture of a double edge notch tension specimen in a nonlinear solid with tension–compression asymmetry (Marked as C3). This kind of specimen is normally used to investigate the fracture behavior of materials with tension–compression symmetry [39]. The geometry setup is shown in Fig. 8a. The initial crack length is  $a = 12$  mm. Due to the symmetry of the specimen, only one half of the specimen is modeled, and is discretized by approximately 30,000 elements and 15,351 nodes, based on a mesh convergence study. The mesh is refined around the initial notch. Compared with [38], we have used increased mesh refinement. The minimum size of elements is 0.66 mm. The dimension of length used in our simulations is 1.5 mm, comparable to the size of two elements. The imposed displacement is increased monotonically. The elastic constants are  $\mu^+ = 0.186$  MPa and  $K^+ = 1.8$  MPa. The fracture toughness is  $\mathcal{G}_c = 1.5$  N/mm and  $\mathcal{K} = 0.01$ .

Fig. 8b plots the reaction force  $F_R$  as a function of the imposed displacement for five modulus ratios between tension and compression ( $\mu^+/\mu^- = 0.2, 0.5, 1.0, 2.0, 5.0$ ). Similar to three-point bending and central cracking, the larger  $\mu^+/\mu^-$  ratio can delay the initiation of the crack propagation. For this example, when the maximum load is reached, the crack propagates rapidly and the stress drops suddenly, as compared to the three-point bending and central cracking in which the stress decreases slower.

Fig. 9a–d shows contours of the nominal stress  $P_{yy}$  and the fracture phase fields at the imposed displacement level  $u = 50$  mm. In comparing our results with [38], we see that Figs. 9a–d are very similar to their results,

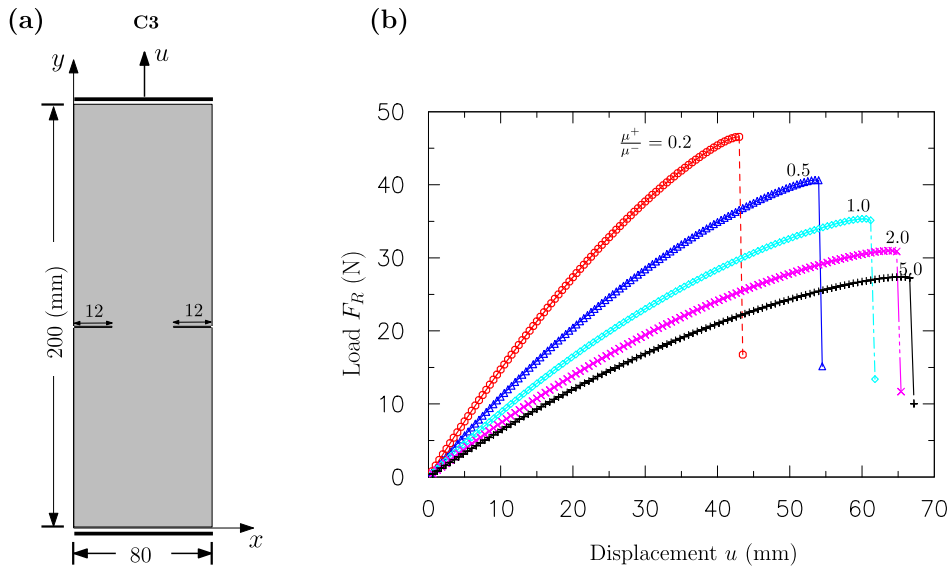


**Fig. 8.** Fracture of a double edge notched specimen under remote tension. (a) Geometry and boundary conditions and (b) the reaction force vs. the imposed displacement under five different levels of modulus ratio:  $\mu^+/\mu^- = 0.2, 0.5, 1.0, 2.0, 5.0$ . The modified neo-Hookean model with tension–compression asymmetry is employed.

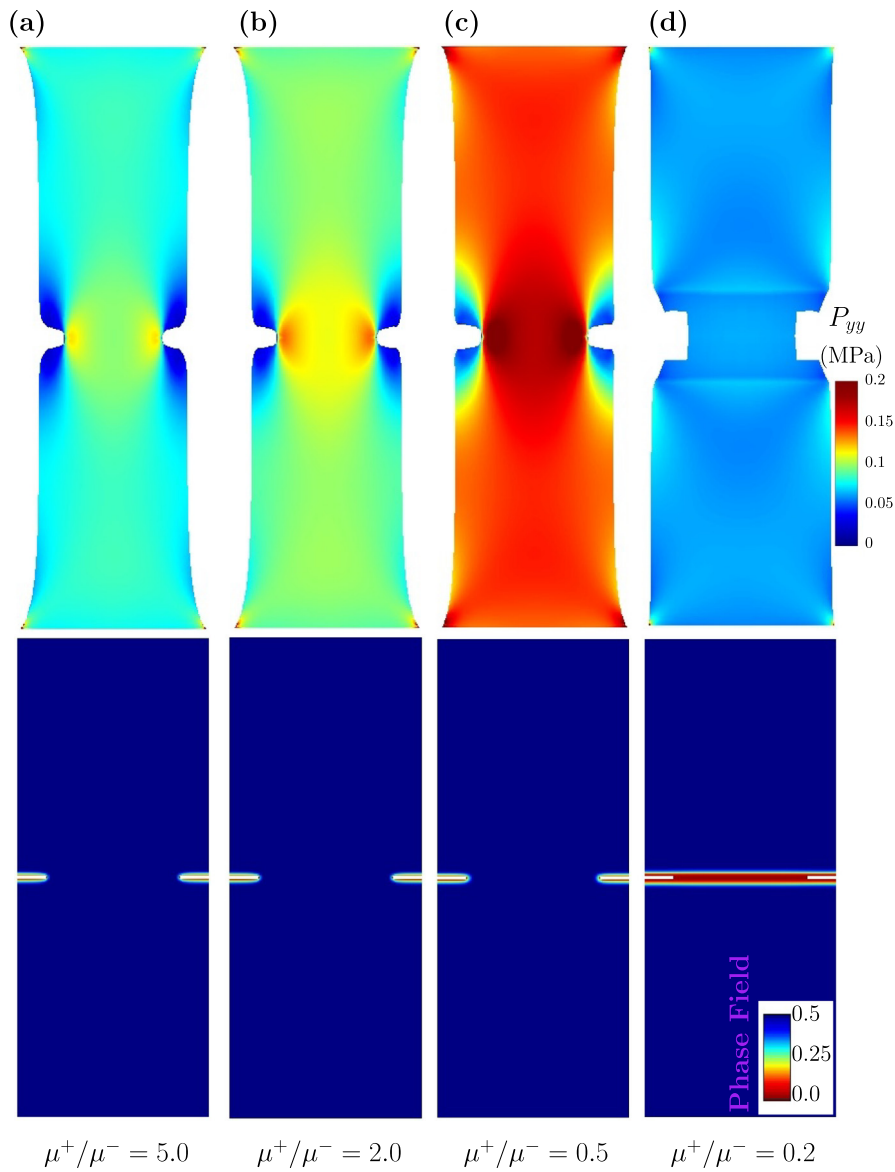
although the tension–compression symmetric materials are used by them. It should be noted that smaller  $\mu^+/\mu^-$  leads to more blunting of the crack tip under the same imposed displacement level, resulting in the longest crack length. The fracture is localized in front of the crack tip, as shown by phase field contour.

We next study the fracture of a porous square specimen (Marked as C4) with the materials of tension–compression asymmetry (neo-Hookean model). The geometry setup and the boundary conditions are shown in Fig. 10a. The lefthand surface is fixed in  $x$  direction and the bottom surface is fixed in  $y$  direction. A part of the righthand surface is displaced in the  $x$  direction. The FE mesh is composed of 15862 elements and 8112 nodes. Values of the shear modulus and bulk modulus taken in the analyses are  $\mu^+ = 1.86$  MPa, and  $K^+ = 18.0$  MPa respectively.  $\mu^+/\mu^- = 0.5$ . The length scale  $\ell$  is set as 0.05 mm, the normalized fracture toughness is  $\mathcal{G}_c = 1.5$  N/mm and  $\mathcal{K} = 0.01$ .

Fig. 10b–c plots the fracture phase field for the problem shown in Fig. 10a at the imposed displacement levels  $u = 0.75$  mm and  $u = 0.98$  mm under  $\mu^+/\mu^- = 0.5$ . In this case. The crack initiates at the bottom boundary, and propagates through the voids towards the right surface with a curved path, different from a straight crack shown in the previous cases. This implies that our method shows a potential to capture complex crack patterns. Additional details of this simulation can be found in an attached movie.

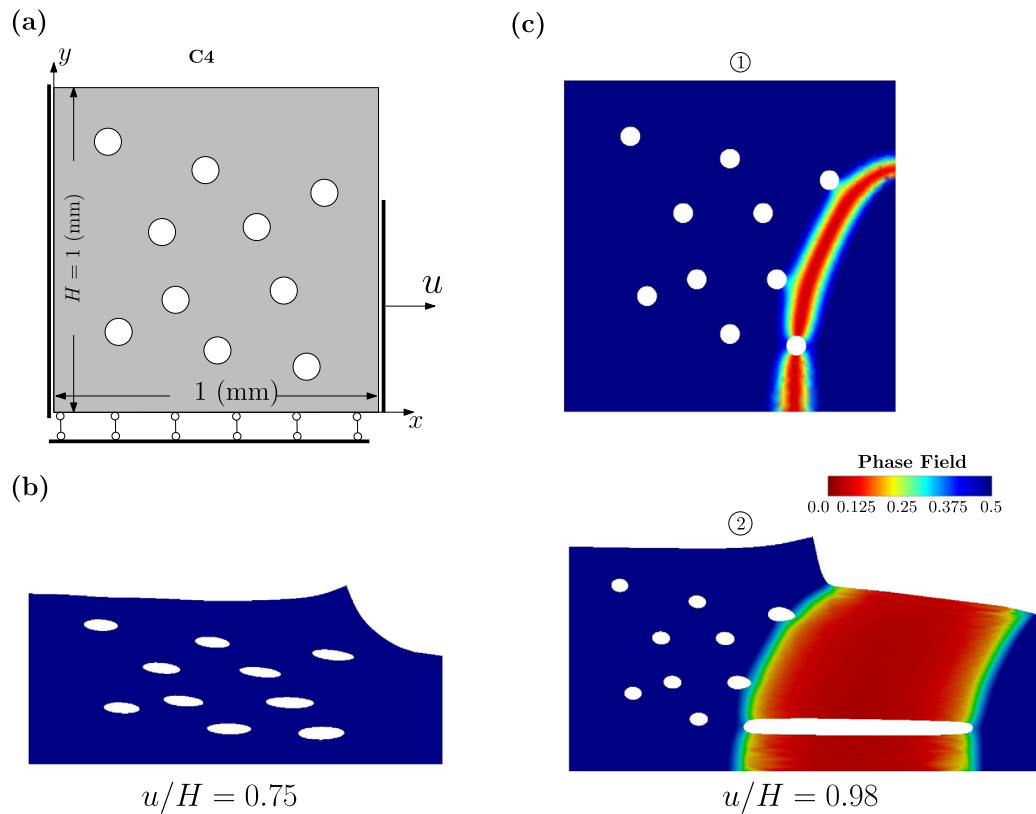
The Odgen model with tension–compression asymmetry (Eq. (1)) is also used in the phase field framework, and compared with the neo-Hookean model. Consider the displacement-controlled quasi-static three-point bending of beam containing a straight vertical notch. The geometry and boundary conditions are shown in Fig. 11a (Marked as C5). Values of the shear modulus and bulk modulus taken in the analyses are  $\mu^+ = 1.86$  MPa and  $K^+ = 18.0$  MPa, respectively. The length scale  $\ell$  is set as 0.02 mm, the normalized fracture toughness  $\mathcal{G}_c/(\mu^+\ell) = 2.016$  and  $\mathcal{K} = 0.001$ .

Fig. 11b plots the reaction force  $F_R$  as a function of normalized displacement  $u/H$  for three different material constant  $\alpha$  (Eq. (1)). Focusing on the effects of the parameter  $\alpha$ , the tension modulus and compression modulus are considered to be same. As shown in Fig. 11b, for different values of the material constant  $\alpha$  ( $\alpha = 2, 3, 5$ ), the force–displacement response is the same at the initial stage of the deformation. With increased displacement, a rapid drop in the force occurs for  $\alpha = 2$  (blue line), followed by a slow decrease. The force drop with  $\alpha = 5$  (red line) occurs at a higher displacement than for  $\alpha = 2$ . After the initial force drop, the force vs displacement curve levels off and then increases slightly.



**Fig. 9.** The contour plots of stress and phase field for a double edge notched specimen in the current deformed and undeformed reference configurations respectively, at the imposed displacement level  $u = 50$  mm under four levels of  $\mu^+/\mu^-$ : (a) 5.0; (b) 2.0; (c) 0.5; (d) 0.2. The modified neo-Hookean model with tension–compression asymmetry is employed.

Fig. 11c shows the stress contours  $P_{xx}$  and the crack phase fields on the deformed and original configurations under the displacement level  $u/H = 1.2$ . Note that  $\alpha$  represents the hardening of material at larger deformation. When  $\alpha$  is small, the propagation of the crack occurs earlier, consistent with what was observed in Fig. 11b. It can be observed that for smaller  $\alpha$ , the crack length is longer under the same imposed displacement. Similar to the stress field of the first example presented, the stress field highly localized around the crack tip. This localized stress field moves with the crack tip as it propagates. The crack propagates more slowly for  $\alpha = 5$  than for  $\alpha = 2$ . One reason is that the fracture process zone with  $\alpha = 5$  is more diffusive, like a spindle. However, the fracture process zone with  $\alpha = 2$  is more like a straight line. The diffusive fracture process zone delays the crack propagation and leads to an increase in force observed in Fig. 11b at the later stage of the fracture. The parameters used in our simulations are also summarized in Table 1.



**Fig. 10.** Fracture of a porous square specimen under uniaxial tension. The modified neo-Hookean model with tension–compression asymmetry is employed. (a) Geometry and boundary conditions and (b) the contour plot of fracture phase field in the current deformed configurations, at the imposed displacement level  $u = 0.75$  mm (c) The contour plots of fracture phase field in the original and current deformed configurations respectively, at the imposed displacement level  $u = 0.98$  mm under  $\mu^+/\mu^- = 0.5$ .

**Table 1**

Values of the parameters used in the simulations.

	$\mu^+$	$K^+$	$\mathcal{G}_c$	$\ell$	$\mathcal{K}$
C1	1.86 MPa	18.0 MPa	0.075 N/mm	0.02 mm	0.001
C2	5.24 MPa	21.0 MPa	1.5 N/mm	0.04 mm	0.001
C3	0.186 MPa	1.8 MPa	1.5 N/mm	1.5 mm	0.01
C4	1.86 MPa	18.0 MPa	1.5 N/mm	0.05 mm	0.01
C5	1.86 MPa	18.0 MPa	0.075 N/mm	0.02 mm	0.001

## 6. Conclusions

In this paper, we have developed an approach for constructing nonlinear elastic material models with tension–compression asymmetry. The proposed approach can avoid the non-zero stress issues by virtue of an appropriate energy decomposition into tensile and compressive parts. The asymmetry is modeled by setting the shear and bulk modulus ratios under tension or compression directly, overcoming the difficulty involved in [9,10]. The present model is also suitable for mixed mode loading and straightforward for finite element implementation, showing the potential to capture the pronounced asymmetry observed in experiments.

The nonlinear elastic material model presented for tension–compression asymmetry has been combined with a phase field approach to simulate the fracture nucleation and crack propagation. In the phase field modeling, the asymmetric effect of tension and compression on fracture is taken into account. The strain energy is decomposed into two parts: the principal stretch and volumetric deformation. This energy decomposition is implemented into

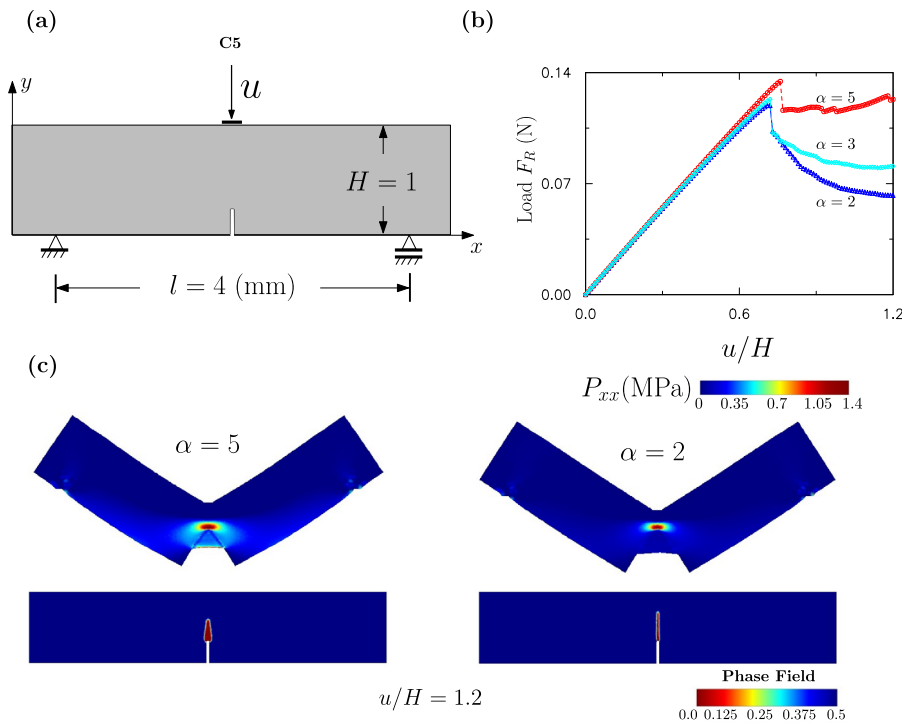


**Fig. 11.** Three-point bending simulations. (a) Geometry and boundary conditions. (b) The reaction force vs. normalized displacement under three different material constant ( $\alpha = 2.0, 3.0, 5.0$ ). (c) The contour plots of stress ( $P_{xx}$ ) and the crack phase field ( $p$ ) for three-point bending specimen in the current deformed and undeformed reference configurations respectively at the imposed displacement  $u/H = 1.2$ . The material constant are  $\alpha = 2$  and  $\alpha = 5$ . The modified Odgen model with tension–compression asymmetry is employed. (For interpretation of the references to color in this figure legend, the reader is referred to the web version of this article.)

the finite element code with numerical stability, and shows the capability of capturing the fracture behavior at finite strain, which has been demonstrated by the fracture nucleation and crack propagation in several typical specimens, including three point bending, and tension of a compact specimen with a centered single notch and double edge notches, respectively. This decomposition can efficiently deal with the deformation with both tension and compression during the fracture process.

It is also found via phase field modeling that the crack tip stress fields for nonlinearly elastic solids with tension–compression asymmetry differ from those with tension–compression symmetry. The stress singularity at the crack tip can be tuned by the ratio of the tension modulus to compression modulus. Smaller compressive modulus can delay fracture propagation. The hardening of the material also can delay the fracture process. This shows a great potential for material design while considering tension–compression asymmetry. The 3D printing may be used to construct nonlinear elastic materials like this, while analyzing crack initiation and propagation.

## Acknowledgments

S.T. appreciates the support from NSF of China (Project No. 11872139). X.G. Thanks the support from NSF of China (11732004, 11821202), and Program for Changjiang Scholars, Innovative Research Team in University (PCSIRT).

## Appendix

The numerical algorithm to solve the phase field fracture on solids with tension–compression asymmetry is summarized in this appendix, see [Box I](#).



**Data:**  $\mathbf{u}_{t-1}$ ,  $p_{t-1}$ , **for**  $t = 0, 1, \dots, N - 1$

**Require:**  $\mathbf{u}_t$ ,  $p_t$

**Define**  $\text{Psign}(y) = \begin{cases} y, & y > 1 \\ 1, & y \leq 1 \end{cases}$        $\text{Nsign}(y) = \begin{cases} y, & y \leq 1 \\ 1, & y > 1 \end{cases}$

**if** neo-Hookean

... Choose the free energy density

$$W = \sum_{i=1}^3 \mu(\lambda_i) \left[ \frac{1}{2} (\lambda_i^2 - 1) - \ln \lambda_i \right] + \frac{K(J)}{2} (\ln J)^2$$

$$\dots W^+ = \sum_{i=1}^3 \mu(\lambda_i) \left[ \frac{1}{2} (\text{Psign}(\lambda_i)^2 - 1) - \ln \text{Psign}(\lambda_i) \right] + \frac{K(J)}{2} (\ln \text{Psign}(J))^2$$

$$\dots W^- = \sum_{i=1}^3 \mu(\lambda_i) \left[ \frac{1}{2} (\text{Nsign}(\lambda_i)^2 - 1) - \ln \text{Nsign}(\lambda_i) \right] + \frac{K(J)}{2} (\ln \text{Nsign}(J))^2$$

**elif** Odgen

... Choose the free energy density

$$W = \sum_{i=1}^3 \left[ \frac{2\mu(\lambda_i)}{\alpha^2} (\lambda_i^\alpha - 1 - \alpha \ln \lambda_i) \right] + \frac{K(J)}{2} (\ln J)^2$$

$$\dots W^+ = \sum_{i=1}^3 \left[ \frac{2\mu(\lambda_i)}{\alpha^2} (\text{Psign}(\lambda_i)^\alpha - 1 - \alpha \ln \text{Psign}(\lambda_i)) \right] + \frac{K(J)}{2} (\ln \text{Psign}(J))^2$$

$$\dots W^- = \sum_{i=1}^3 \left[ \frac{2\mu(\lambda_i)}{\alpha^2} (\text{Nsign}(\lambda_i)^\alpha - 1 - \alpha \ln \text{Nsign}(\lambda_i)) \right] + \frac{K(J)}{2} (\ln \text{Nsign}(J))^2$$

**for** every successive load step  $n+1$

... **Initialization:**  $(\mathbf{u}_t^{(0)}, p_t^{(0)}) = (\mathbf{u}_{t-1}, p_{t-1})$

... **While**  $err > tol$

..... Calculate  $\mathbf{u}_t^{(k+1)}$  with frozen fracture phase field  $p_t^{(k)}$  using Eq. (11)

..... with the first P-K stress

$$P_{iJ} = \left[ (1 - \mathcal{K}) p_t^{(k)^2} + \mathcal{K} \right] \frac{\partial W^+(\mathbf{u}_t^{(k+1)})}{\partial F_{iJ}} + \frac{\partial W^-(\mathbf{u}_t^{(k+1)})}{\partial F_{iJ}}$$

..... Calculate the phase field  $p_t^{(k+1)}$  with fixed displacements  $\mathbf{u}_t^{(k+1)}$  using Eq. (12)

..... subjected to:  $0 \leq p_t^{(k+1)} \leq p_t^{(k)} \leq 1$

.....  $err = \|p_t^{(k+1)} - p_t^{(k)}\|_\infty$

..... Set  $k = k + 1$

... Update unknowns:  $(\mathbf{u}_t, p_t) = (\mathbf{u}_t^{(k)}, p_t^{(k)})$

**Box I.** Solving Scheme for Phase Field Fracture on Solids with Tension–Compression Asymmetry.

## Appendix B. Supplementary data

Supplementary material related to this article can be found online at <https://doi.org/10.1016/j.cma.2019.112573>.

## References

- [1] K. Miller, K. Chinzei, Constitutive modelling of brain tissue: experiment and theory, *J. Biomech.* 30 (11–12) (1997) 1115–1121.
- [2] K.L. Thibault, S.S. Margulies, Age-dependent material properties of the porcine cerebrum: effect on pediatric inertial head injury criteria, *J. Biomech.* 31 (12) (1998) 1119–1126.
- [3] M.T. Prange, S.S. Margulies, Regional, directional, and age-dependent properties of the brain undergoing large deformation, *J. Biomech. Eng.* 124 (2) (2002) 244–252.



- [4] K. Miller, K. Chinzei, Mechanical properties of brain tissue in tension, *J. Biomech.* 35 (4) (2002) 483–490.
- [5] F. Velardi, F. Fraternali, M. Angelillo, Anisotropic constitutive equations and experimental tensile behavior of brain tissue, *Biomech. Model. Mechanobiol.* 5 (1) (2006) 53–61.
- [6] B. Rashid, M. Destrade, M.D. Gilchrist, Mechanical characterization of brain tissue in compression at dynamic strain rates, *J. Mech. Behav. Biomed. Mater.* 10 (1) (2012) 23–38.
- [7] B. Rashid, M. Destrade, M.D. Gilchrist, Mechanical characterization of brain tissue in simple shear at dynamic strain rates, *J. Mech. Behav. Biomed. Mater.* 28 (1) (2013) 71–85.
- [8] B. Rashid, M. Destrade, M.D. Gilchrist, Mechanical characterization of brain tissue in tension at dynamic strain rates, *J. Mech. Behav. Biomed. Mater.* 33 (1) (2014) 43–54.
- [9] S. Budday, G. Sommer, C. Birkel, C. Langkammer, J. Haybaeck, J. Kohnert, M. Bauer, F. Paulsen, P. Steinmann, E. Kuhl, Mechanical characterization of human brain tissue, *Acta Biomater.* 48 (2017) 319–340.
- [10] S. Budday, G. Sommer, J. Haybaeck, P. Steinmann, G. Holzapfel, E. Kuhl, Rheological characterization of human brain tissue, *Acta Biomater.* 60 (2017) 315–329.
- [11] M.P. Alexander, Mild traumatic brain injury: pathophysiology, natural history, and clinical management, *Neurology* 45 (7) (1995) 1253–1260.
- [12] M. Inglese, S. Makani, G. Johnson, B.A. Cohen, J.A. Silver, O. Gonen, R.I. Grossman, Diffuse axonal injury in mild traumatic brain injury: a diffusion tensor imaging study, *J. Neurosurgery* 103 (2) (2005) 298–303.
- [13] M. Faul, L. Xu, M. Wald, V. Coronado, A. Dellinger, Traumatic brain injury in the united states: national estimates of prevalence and incidence, *Injury Prevention* 16 (Suppl 1) (2010) A268.
- [14] L. Young, G.T. Rule, R.T. Bocchieri, Walilko, When physics meets biology: Low and high-velocity penetration, blunt impact, and blast injuries to the brain, *Front. Neurol.* 6 (2015) 89.
- [15] M. Hemphill, S. Dauth, Y. Chung Jong, B. Dabiri, Traumatic brain injury and the neuronal microenvironment: A potential role for neuropathological mechanotransduction, *Neuron* 85 (6) (2015) 1177–1192.
- [16] B.K. Eyal, M.T. Scimone, J.B. Estrada, F. Christian, Strain and rate-dependent neuronal injury in a 3D *in vitro* compression model of traumatic brain injury, *Sci. Rep.* 6 (2016) 30550.
- [17] S. Ambartsumyan, The axisymmetric problem of circular cylindrical shell made of materials with different stiffness in tension and compression, *Izv. Akad. Nauk SSSR Mekh.* 4 (4) (1965) 77–85.
- [18] S. Ambartsumyan, A. Khachatryan, The basic equations of the theory of elasticity for materials with different tensile and compressive stiffness, *Mech. Solids* 1 (2) (1966) 29–34.
- [19] S. Ambartsumyan, *Elasticity Theory of Different Moduli*, China Railway Publishing House, Beijing, 1986.
- [20] Z. Du, X. Guo, Variational principles and the related bounding theorems for bi-modulus materials, *J. Mech. Phys. Solids* 73 (2014) 183–211.
- [21] Z. Du, Y. Zhang, W. Zhang, X. Guo, A new computational framework for materials with different mechanical responses in tension and compression and its applications, *Int. J. Solids Struct.* 100 (2016) 54–73.
- [22] G.A. Francfort, J.J. Marigo, Revisiting brittle fracture as an energy minimization problem, *J. Mech. Phys. Solids* 46 (8) (1998) 1319–1342.
- [23] C. Miehe, M. Hofacker, F. Welschinger, A phase field model for rate-independent crack propagation: Robust algorithmic implementation based on operator splits, *Comput. Methods Appl. Mech. Engrg.* 199 (45) (2010) 2765–2778.
- [24] C. Miehe, F. Welschinger, M. Hofacker, Thermodynamically consistent phase-field models of fracture: variational principles and multi-field FE implementations, *Internat. J. Numer. Methods Engrg.* 83 (10) (2010) 1273–1311.
- [25] H. Amor, J.J. Marigo, C. Maurini, Regularized formulation of the variational brittle fracture with unilateral contact: Numerical experiments, *J. Mech. Phys. Solids* 57 (8) (2009) 1209–1229.
- [26] C.J. Larsen, C. Ortner, Existence of solutions to a regularized model of dynamic fracture, *Math. Models Methods Appl. Sci.* 20 (07) (2010) 1021–1048.
- [27] C.J. Larsen, *Models for Dynamic Fracture Based on Griffith’s Criterion*, Springer Netherlands, 2010, pp. 131–140.
- [28] B. Bourdin, C.J. Larsen, C.L. Richardson, A time-discrete model for dynamic fracture based on crack regularization, *Int. J. Fract.* 168 (168) (2010) 133–143.
- [29] M.J. Borden, C.V. Verhoosel, M.A. Scott, T.J.R. Hughes, C.M. Landis, A phase-field description of dynamic brittle fracture, *Comput. Methods Appl. Mech. Engrg.* 217 (1) (2012) 77–95.
- [30] M. Hofacker, C. Miehe, A phase field model of dynamic fracture: Robust field updates for the analysis of complex crack patterns, *Internat. J. Numer. Methods Engrg.* 93 (3) (2013) 276–301.
- [31] S. Tang, G. Zhang, T.F. Guo, X. Guo, W.K. Liu, Phase field modeling of fracture in nonlinearly elastic solids via energy decomposition, *Comput. Methods Appl. Mech. Engrg.* 347 (2019) 477–494.
- [32] C. Miehe, S. Göktepe, F. Lulei, A micro-macro approach to rubber-like materials-part i: the non-affine micro-sphere model of rubber elasticity, *J. Mech. Phys. Solids* 52 (11) (2004) 2617–2660.
- [33] S. Tang, S. Greene, W.K. Liu, Two-scale mechanism-based theory of nonlinear viscoelasticity, *J. Mech. Phys. Solids* 60 (2) (2012) 199–226.
- [34] Y. Li, S. Tang, M. Kröger, W.K. Liu, Molecular simulation guided constitutive modeling on finite strain viscoelasticity of elastomers, *J. Mech. Phys. Solids* 88 (2016) 204–226.
- [35] L. Rosati, N. Valoroso, A return map algorithm for general isotropic elasto/viscoplastic materials in principal space, *Internat. J. Numer. Methods Engrg.* 60 (2) (2004) 461–498.
- [36] S. Tang, Y. Yang, X.H. Peng, W.K. Liu, X.X. Huang, K. Elkhodary, A semi-numerical algorithm for instability of compressible multilayered structures, *Comput. Mech.* 56 (1) (2015) 63–75.

- [37] C. Miehe, L.M. Schänzel, H. Ulmer, Phase field modeling of fracture in multi-physics problems. part i. balance of crack surface and failure criteria for brittle crack propagation in thermo-elastic solids, *Comput. Methods Appl. Mech. Engrg.* 294 (1) (2015) 449–485.
- [38] C. Miehe, L.M. Schänzel, Phase field modeling of fracture in rubbery polymers. part i: Finite elasticity coupled with brittle failure, *J. Mech. Phys. Solids* 65 (5) (2014) 93–113.
- [39] N.A. Hocine, M.N. Abdelaziz, A. Imad, Fracture problems of rubbers: J-integral estimation based upon  $\eta$  factors and an investigation on the strain energy density distribution as a local criterion, *Int. J. Fract.* 117 (1) (2002) 1–23.